



Anatomy and Impact of a High Arctic Atmospheric River Driving Extreme Winter Rain and Snowfall

Hannah Bailey¹, Jason E. Box², Ben G. Kopec³, Valtteri Hyöky¹, Hannu Marttila¹, Jeffrey M. Welker^{4,5}, Jack Kohler⁶, Dmitry V. Divine⁶, and Alun Hubbard^{7,8}

- 5 ¹Water, Energy, and Environmental Engineering Research Unit, University of Oulu, 90014 Oulu, Finland
²Department of Glaciology and Climate, Geological Survey of Denmark and Greenland, 1350 Copenhagen, Denmark
³Great Lakes Research Center, Michigan Technological University, Houghton, MI 49931, USA
⁴Ecology and Genetics Research Unit, University of Oulu, 90014 Oulu, Finland
⁵Department of Biological Sciences, University of Alaska Anchorage, Anchorage, AK 99508, USA
10 ⁶Norwegian Polar Institute, 9296 Tromsø, Norway
⁷Geography Research Unit, University of Oulu, 90014 Oulu, Finland
⁸Department of Geosciences, UiT - The Arctic University of Norway, 9037 Tromsø, Norway

Correspondence to: Hannah Bailey (hannah.bailey@oulu.fi)

15 **Abstract.** Atmospheric rivers (ARs) transport concentrated fluxes of heat and moisture poleward, driving temperature and precipitation extremes. Yet, their vertical structure in the High Arctic – where small thermodynamic perturbations govern rain-snow partitioning and cryospheric response – remains poorly constrained. Here we present atmospheric vapour isotope, radiosonde, and meteorological observations from Svalbard during a record-setting AR in March 2022. The AR developed in the northwest Atlantic when a deep “bomb” cyclone established a sustained conduit of poleward heat/moisture. Integrated
20 vapour transport exceeded $450 \text{ kg m}^{-1} \text{ s}^{-1}$, with warming and enhanced moisture emerging $\sim 2\text{--}6$ km aloft before deepening through the lower-troposphere, tripling near-surface humidity. On 15 March, air temperatures rose to $5.6 \text{ }^\circ\text{C}$ accompanied by 43.9 mm rainfall – the highest daily March total on record. Concurrently, vapour $\delta^{18}\text{O}$ (d-excess) attained its campaign maximum (minimum) and marine aerosol (Na^+) concentrations spiked, constraining the geochemical signature of Atlantic moisture advection. The two-day AR event delivered $\sim 0.5 \text{ Gt}$ snowfall across Svalbard, locally equivalent to over 8% of net
25 2022 glacier accumulation and offsetting surface mass loss by $\sim 7\%$. Although rainfall comprised less than one-third of the total precipitation, it impacted 60% of the glacierised terrain, driving winter rain-on-snow melt and densification across lower-elevation areas and altering snowpack structure. Our study underscores the vulnerability of Svalbard and other glacierised Arctic archipelagos to intensifying poleward moisture and heat transport by ARs, with substantial but nuanced impacts on glacier surface energy budget and mass balance through the delivery of anomalous winter rainfall, snowfall, and latent heat.

30 1 Introduction

Atmospheric rivers (ARs) play a critical role in the global climate system, conveying high fluxes of heat, moisture, and momentum into higher latitudes (Wang et al., 2024). In polar regions, this advection can trigger pronounced temperature and

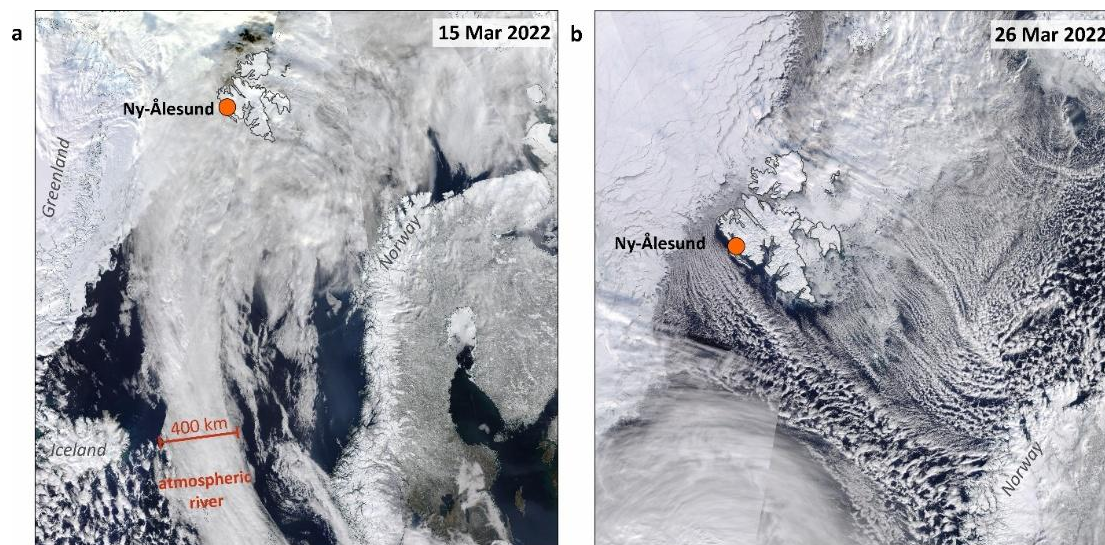
precipitation anomalies (Payne et al., 2020; Scholz and Lora, 2024) including extreme rainfall (Box et al., 2023), snowfall (Bailey and Hubbard, 2025; Gorodetskaya et al., 2014), and rain-on-snow (ROS) events (Box et al., 2022; Sobota et al., 2020).

35 These anomalies can modify snowpack structure (Salzano et al., 2023; Sobota et al., 2020) and modulate radiative and turbulent fluxes (Mattingly et al., 2020), with consequences for sea-ice growth (Hegyi and Taylor, 2018; Zhang et al., 2023) and ice-sheet mass balance (Bailey and Hubbard, 2025; Mattingly et al., 2018; Wedum et al., 2026).

Recent work highlights contrasting impacts of ARs on the Antarctic and Greenland ice sheets, where large AR-fuelled snowfall events can substantially enhance surface mass balance at high elevations (Adusumilli et al., 2021; Bailey and Hubbard, 2025; Gorodetskaya et al., 2014; MacLennan et al., 2022), whereas rainfall is increasingly linked to widespread surface melt and mass loss (Box et al., 2022; Gorodetskaya et al., 2023; Mattingly et al., 2020, 2023). Despite these insights, the vertical thermodynamic structure of polar ARs – and how it governs the partitioning of precipitation between rain and snow – remain poorly constrained by direct observations. This gap is particularly acute across mid- to high-latitude maritime glaciated regions with complex topography (Nygård et al., 2016; Payne et al., 2020), where warm air intrusions can raise winter surface air temperatures (SATs) above freezing. In such settings, small thermodynamic perturbations can critically modulate precipitation phase (Bintanja and Andry, 2017), with disproportionate consequences for seasonal snowpacks (Peeters et al., 2019), low-lying maritime glaciers (Noël et al., 2020), and the timing and magnitude of downstream hydrological and biogeochemical fluxes (Croghan et al., 2025; Kleber et al., 2025). Consequently, how AR-driven moisture transport translates into rain versus snowfall across short spatial scales remains poorly resolved, limiting process-level understanding of hydroclimatic impacts in polar maritime regions.

The Svalbard archipelago is an Arctic hotspot where mean rates of warming have exceeded 1.25 °C per decade since 1979 (Rantanen et al., 2022). Situated directly in the path of poleward-advecting Atlantic air masses, it occupies a critical position for studying ARs which contribute disproportionately to over 40% of annual precipitation (2017-2021) (Ebell et al., 2025). Approximately ~60% of the archipelago is glacierised (~36,500 km²), with an estimated volume of 6,800 ± 238 km³ (Van Pelt and Frank, 2025) distributed among its 1666 glaciers (RGI 7.0 Consortium, 2023). Between 2002 and 2023, their mean mass deficit was 14.8 ± 1.3 gigatonnes (Gt) yr⁻¹ (Sasgen et al., 2024), with a forecast doubling of ice loss by 2100 (Geyman et al., 2022). This combination of strong Atlantic influence, marginal winter thermal conditions, and ongoing mass loss makes Svalbard an ideal natural laboratory for examining how extreme AR moisture transport manifests in the High Arctic.

Here, we present a detailed empirical analysis of a record-setting AR event that made landfall in Svalbard during mid-March 2022 (Fig. 1a). The event drove anomalously high SATs and precipitation across a large sector of the Arctic (Bailey and Hubbard, 2025; Walbröl et al., 2024), and was followed by an intense marine cold air outbreak (CAO) (Kirbus et al., 2024) (Fig. 1b). We captured this extreme AR-CAO sequence using continuous measurements of atmospheric water vapour isotopes (δ¹⁸O, δ²H) at Ny-Ålesund, northwest Svalbard, together with upper-air radiosonde observations and meteorological data, providing rare observational constraints on the moisture provenance, thermodynamic structure, and surface coupling of the event.



70 **Figure 1: Satellite images during mid-March 2022.** Aqua-MODIS satellite images on (a) 15 March 2022 showing the North Atlantic AR transiting between Iceland/Greenland and Scandinavia toward Ny-Ålesund, Svalbard (orange circle), and (b) on 26 March 2022 during the CAO showing ‘cloud streets’ forming off the Arctic Ocean sea ice in the Fram Strait and Barents Sea. Imagery from NASA Worldview.

2 Methods

75 2.1 Stable isotope measurements

Atmospheric water vapour isotopes ($^{18}\text{O}/^{16}\text{O}$ and $^2\text{H}/^1\text{H}$) and mixing ratios were measured continuously between 1 January and 31 May 2022 at the NPI Zeppelin Observatory (78.91°N , 11.89°E ; 475 m a.s.l.) in Ny-Ålesund. Ambient air was sampled through approximately 3 m of inlet tubing drawing air from above the roof of the laboratory building. To limit residence time the air was pumped through the line at a flow rate of 3 L min^{-1} , giving a residence time of ~ 3 seconds from the inlet to the analyser. A low-energy heating cable was wrapped around the inlet to prevent freezing, and a shield was used to stop precipitation from entering the sampling line. Temperature inside the laboratory was maintained at 20°C throughout the campaign to ensure instrument stability and prevent condensation in the line.

Stable isotope ratios ($\delta^{18}\text{O}$ and $\delta^2\text{H}$) were measured approximately every second using a cavity ring-down spectrometer (Picarro L2130-i, Picarro Inc., USA). The analyser was connected to a Picarro Standards Delivery Module supplying two reference waters with known isotopic composition approximately every 24 h (Ala-Aho et al., 2021). Calibration standards USGS-45 ($\delta^{18}\text{O} = -2.238\text{‰}$, $\delta^2\text{H} = -10.3\text{‰}$) and USGS-49 ($\delta^{18}\text{O} = -50.55\text{‰}$, $\delta^2\text{H} = -394.7\text{‰}$), which span the isotopic range of ambient measurements during the campaign, were used to correct measurements to the VSMOW-SLAP scale and monitor instrumental drift. Stable isotope data were calibrated and corrected for humidity using standard established protocols (Madsen et al., 2019). Standard waters were measured across a range of controlled water vapour concentrations to establish a humidity response function, which was subsequently applied to the dataset (Bailey et al., 2021; Freitas et al., 2024). Following

calibration and quality control procedures, isotope measurements were aggregated to 5 min averages. Analytical uncertainty is estimated to be $<0.3\%$ for $\delta^{18}\text{O}$ and $<1.1\%$ for $\delta^2\text{H}$ – considerably smaller than the natural variability observed during the March 2022 AR.

95

Twenty-four snowfall samples were collected at the Ny-Ålesund Research Station–Sverdrup during the measurement campaign and analysed for $\delta^{18}\text{O}$ and $\delta^2\text{H}$ at the FARLAB (University of Bergen, Norway). Samples were transferred to 1.5 mL septa-capped glass vials prior to analysis and measured using a Picarro L2140-i Cavity-Ring Down Spectrometer coupled to an autosampler (Picarro A0325) and high-precision vaporiser (Picarro A0211). For each sample, repeated injections of ~ 2 μL of liquid water were vaporised at $\sim 110\text{ }^\circ\text{C}$ and introduced into the spectrometer cavity with dry N_2 carrier gas, producing water vapour concentrations of $\sim 20,000$ ppm during analysis. Multiple injections (6-12) were performed for each sample to minimise memory effects, and the final isotope value was calculated from the mean of the final injections after equilibration (Mellat et al., 2021). Isotope ratios are reported in δ -notation relative to the VSMOW-SLAP scale following standard laboratory calibration procedures (Akers et al., 2024; Bailey et al., 2018). Mean analytical uncertainty is 0.05% for $\delta^{18}\text{O}$, 0.5 $\%$ for $\delta^2\text{H}$, and 0.6% for d-excess.

100

105

2.2 Radiosonde observations

Radiosonde profiles are derived from six-hourly launches from the French-German AWIPEV Research Base in Ny-Ålesund (78.92°N , 11.92°E , 17 m a.s.l.) using a Vaisala RS41 radiosonde (Maturilli, 2022). Specific humidity was derived from measurements of air temperature (T), relative humidity (RH) and pressure (p). Integrated water vapour (IWV) was calculated by vertically integrating specific humidity in pressure coordinates over the full available radiosonde profile, and is reported in units of kg m^{-2} , equivalent to millimetres of precipitable water.

110

Wet-bulb temperature (T_w) was calculated from radiosonde measurements of T, RH, and p using a standard pressure-dependent psychrometric formulation (Davies-Jones, 2008). The melting level was defined as the height of the surface-connected $T_w = 0\text{ }^\circ\text{C}$ crossing, obtained by linear interpolation between adjacent levels. Uncertainty in T_w was estimated through propagation of radiosonde measurement uncertainties ($\pm 0.2\text{--}0.4\text{ K}$ in T; $\pm 3\text{--}4\%$ in RH) (Maturilli, 2022), yielding T_w uncertainties of $0.27\text{--}0.46\text{ }^\circ\text{C}$. Given the observed vertical gradient of T_w near the melting level ($\sim 5.5\text{ }^\circ\text{C km}^{-1}$), this corresponds to an uncertainty in melting-level height of approximately $\pm 50\text{--}80\text{ m}$. We note the reconstructed melting-level closely tracks observed precipitation phase at Ny-Ålesund.

115

120 2.3 Meteorological, reanalysis, and glacier data

Hourly surface meteorological observations are utilised from Ny-Ålesund (SN99910; 78.9218°N , 11.9325°E , 8 m a.s.l.), Svalbard Airport (No. SN99840; 78.2453°N , 15.5015°E , 28 m a.s.l.), Adventdalen (SN99870; 78.2022°N , 15.831°E , 15 m a.s.l.), and Hornsund (SN99754; 77.0002°N , 15.5353°E , 10 m a.s.l.) meteorological stations (<https://seklima.met.no/>). We also

125 utilise daily sodium (Na^+) aerosol concentrations measured at the Zeppelin Observatory in Ny-Ålesund (EBAS database, NILU).

130 Synoptic meteorological and surface conditions are examined using ERA5 reanalysis fields produced by the European Centre for Medium-Range Weather Forecasts (ECMWF). Daily statistics on single levels (1940 to present) were retrieved from the Copernicus Climate Data Store and include 2m air temperature, mean sea level pressure, total precipitation, snowfall, snowmelt, total column water vapour (IWV), skin temperature, surface thermal radiation downwards (LWD), and surface latent heat flux (LHF). Hourly geopotential at 850 hPa was retrieved from the ERA5 hourly data on pressure levels dataset. The vertical integrals of eastward and northward water vapour flux were used as the two vector components of integrated vapour transport (IVT) shown in Figure 2 and obtained from EDARA: An ERA5-based Dataset for Atmospheric River Analysis (Mo, 2024).

135 Vertical profiles of Copernicus Arctic Regional ReAnalysis (CARRA) data (single levels from 1991 to present, East domain) were analysed along a horizontal transect from 72.47 °N, 3.48 °W to 81.61 °N, 30.00 °W, chosen to intersect Ny-Ålesund and the NW glacier region of Svalbard approximately along the southwest-northeast axis of the AR. Variables include 3-hourly averages of wind speed, temperature, pressure, and cloud liquid water content on pressure levels between 1000 and 400 hPa. 140 We note that while CARRA provides higher spatial resolution and is therefore used here to examine the dynamical structure of the AR in cross-section; ERA5 was retained for precipitation and surface energy analyses to ensure consistency with the 1981-2010 climatological baseline, which predates the start of the CARRA record.

145 Glacier outlines from the Randolph Glacier Inventory v7.0 (RGI Region 07: Svalbard and Jan Mayen) are used to quantify ERA5 precipitation and snowmelt fields across glacier basins. Rainfall was estimated as the difference between total precipitation and snowfall at each grid cell. Water-equivalent depths were converted to total mass using the glacierised area of each basin. Precipitation and snowmelt volumes were calculated as $M = A \times d$, where M is water mass, A is glacier area, and d is water-equivalent depth. Mass values were converted to gigatonnes (Gt), where 1 Gt = 10^9 m³ of water equivalent.

150 3 Results

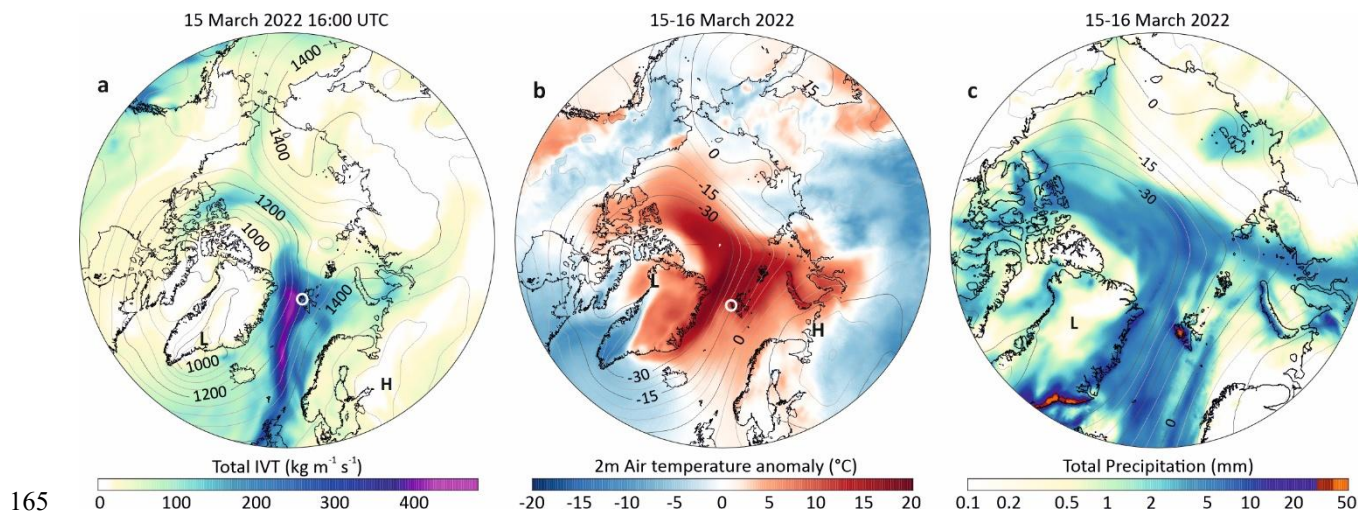
3.1 Atlantic bomb cyclogenesis and AR development

155 The March 2022 AR developed in response to rapid cyclogenesis in the northwest Atlantic, culminating in an explosively deepening low-pressure system over southern Greenland. By 15 March, the cyclone had intensified to a core sea-level pressure (SLP) below 945 hPa near the Denmark Strait. Concurrently, a persistent ridge of high pressure (>1020 hPa) over Scandinavia established a strong meridional pressure gradient across the North Atlantic-Arctic sector (Fig. 2), consistent with a Scandinavian blocking pattern (Lapointe et al., 2024).

This synoptic configuration generated a ~400 km-wide corridor of enhanced integrated vapour transport (IVT) along the eastern flank of the cyclone, extending from the North Atlantic through the Greenland Sea and Fram Strait toward Svalbard



160 (Fig. 1a and 2a). ERA5 data (Hersbach et al., 2020; Mo, 2024) indicate northward IVT exceeded $\sim 400\text{--}500 \text{ kg m}^{-1} \text{ s}^{-1}$ as the AR propagated poleward, classifying the event as *very strong* for the Arctic (Walbröl et al., 2024). Tightly packed geopotential height contours along the AR core reflect strong low-level winds sustaining efficient horizontal moisture transport into the High Arctic (Fig. 2a).



165

Figure 2: Synoptic setting during the March 2022 AR. (a) Total integrated vapour transport (IVT) at 16:00 UTC on 15 March with corresponding 850mb geopotential height contours; (b) mean 2m air temperature (shading) and SLP anomalies (contours) on 15–16 March; and (c) total precipitation between 15-16 March (shading) with corresponding SLP anomalies (contours). All anomalies are relative to the 1981-2010 baseline. The white circle in (a and b) indicates Ny-Ålesund, Svalbard. High (H) and low (L) pressure centres are indicated. Data derive from ERA5 reanalysis (Hersbach et al., 2020). Base maps derive from the ETOPO5 gridded dataset (<http://www.ngdc.noaa.gov/mgg/global/etopo5.HTML>).

170

Poleward advection of warm, mid-latitude air produced exceptional lower-tropospheric thermodynamic anomalies. Mean 2 m SAT anomalies on 15-16 March exceeded $+20 \text{ }^{\circ}\text{C}$ across a large swathe of the Central Arctic Ocean and the Greenland and Barents Seas relative to the 1981–2010 climatology (Fig. 2b). These anomalies coincided with widespread positive precipitation departures along the AR pathway, with cumulative totals exceeding 45 mm over parts of southeast Greenland, Iceland, and western Svalbard between 15 and 16 March (Fig. 2c) (Hersbach et al., 2020).

175

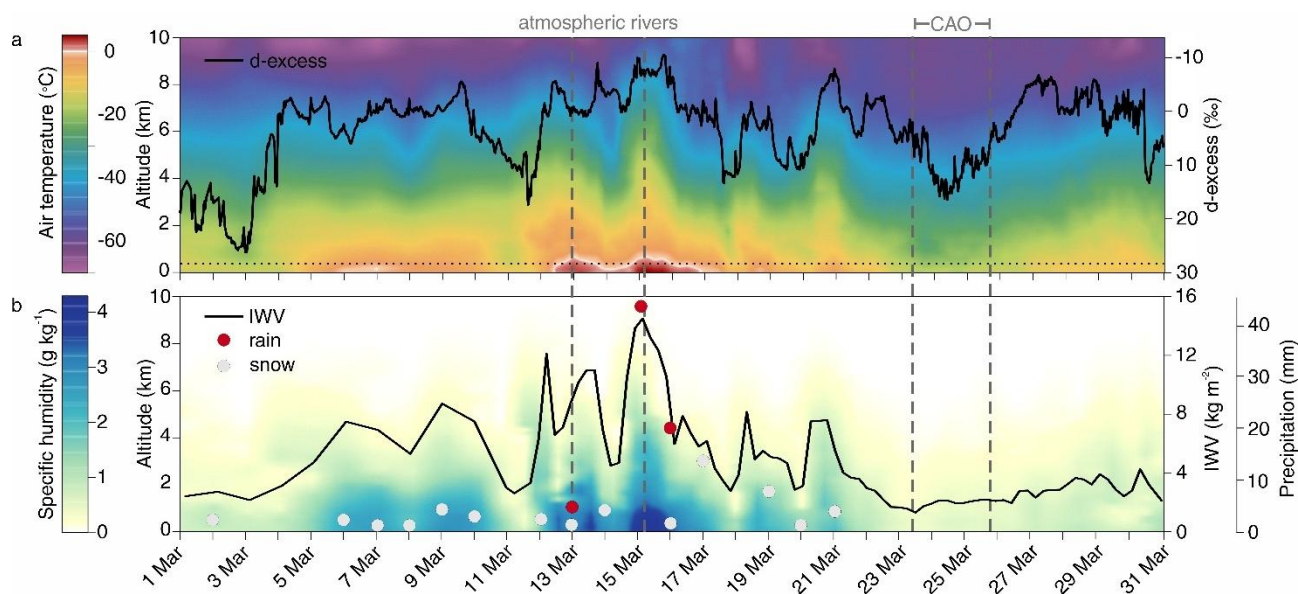
3.2 Anatomy of an Arctic AR

180

AR cross sections using CARRA data reveal a low-level jet transporting a $\sim 2 \text{ km}$ -deep, moisture-laden flow toward Svalbard (Fig. 3). Winds peaked near 925 hPa at $>28 \text{ m s}^{-1}$ and were similarly strong above the complex terrain of NW Svalbard, where turbulent flow prompted extreme uplift and downdrafts (Fig. 3a). Turbulence was most pronounced in the lowest levels, where



190 Embedded within the AR was a ~1.8 km-deep liquid-bearing moisture plume with cloud liquid water content (LWC) reaching 0.05 g kg⁻¹ (Fig. 3b). Pseudo-adiabatic potential temperature (θ_{pe}) surfaces – indicating the tendency for inertial and buoyant motion – slope upward toward the terrain, indicating buoyant ascent from condensation associated with enhanced precipitation alongside terrain-forced uplift. The θ_{pe} contours exhibit undulations with horizontal wavelengths of ~10-50 km, consistent with orographically forced gravity waves generated as stably stratified flow interacts with the mountainous terrain of NW Svalbard. Downstream of the Holtedahlfonna ice cap (~1,200 m a.s.l.), cloud LWC declines sharply (Fig. 3b), indicating moisture
 195 depletion in the lee-side flow. The temperature cross section reveals a pronounced warm lower troposphere during the AR, with near-surface temperatures exceeding 4 °C with sub-freezing temperatures largely confined above ~750 m a.s.l. (Fig. 3c). Radiosondes launched every six hours from Ny-Ålesund (17 m a.s.l) capture this evolving upper-air thermodynamic structure during the AR and subsequent CAO (Fig. 4) (Maturilli, 2022). Prior to AR arrival, the atmospheric column was uniformly
 200 cold, with near-surface temperatures of ~-15 °C decreasing to below -60 °C by ~10 km altitude (Fig. 4a). Integrated water vapour (IWV) remained low (<3 kg m⁻²), consistent with the dry Arctic background state.



205 **Figure 4: Vertical structure of the March 2022 AR and CAO at Ny-Ålesund. (a)** Interpolated radiosonde air temperature (shading) with vapour d-excess (black line; axis reversed). The horizontal dotted line marks the Zeppelin Observatory altitude; **(b)** specific humidity (shading) with integrated water vapour (IWV; black line) and daily precipitation (circles; rain in red, snow in grey). Soundings were launched from Ny-Ålesund (Maturilli, 2022), and the altitude axes are limited to 10km. Vertical dashed lines indicate AR and CAO periods.

The first signature of AR influence appeared aloft around midday on 11 March, when warming initiated between ~2-6 km altitude (Fig. 4a), indicating the arrival of warm maritime air overrunning the cold Arctic boundary layer. Over the following
 210 12 h this warm anomaly deepened downward, progressively displacing the near-surface cold layer. By late 12 March, near-



surface temperatures exceeded 0 °C (Fig. 3e), with above-freezing temperatures extending to ~0.7 km altitude (Fig. 4a), substantially reducing the low-level lapse rate and effectively coupling warm maritime air to the surface.

215 Simultaneously, IWV increased rapidly and developed a double-peaked structure during 12-13 March, rising approximately four-fold from pre-AR values to maxima of 12.1 and 11.0 kg m⁻² (Fig. 4b). Specific humidity profiles indicate that this increased corresponded to the arrival of the moisture plume, initially confined above ~4.8 km before progressively descending into the lower troposphere. As the plume deepened, mean specific humidity within the lowest kilometre increased to ~3.6 g kg⁻¹, with the two IWV pulses indicating episodic low-level moisture delivery during the early AR phase (Fig. 4b).

220 The AR intensified on 15 March, producing the strongest thermodynamic and moisture anomalies of the event (Fig. 4). Near-surface temperatures reached 5.6 °C, with above-freezing conditions extending to ~0.8 km altitude (Fig. 4a). IWV peaked at 14.6 kg m⁻² – the highest March value in the 1993-2022 radiosonde record (Maturilli, 2022) – while specific humidity exceeded ~4 g kg⁻¹ through the lowest kilometre for more than 24 h (Fig. 4b). Elevated moisture transport persisted until 16 March, coincident with extreme rainfall and low vapour d-excess measured in Ny-Ålesund (Fig. 5a-b).

225 From 23 March onward, radiosoundings record the transition to markedly cooler and drier conditions. The lower and mid-troposphere cooled, with near-surface temperatures falling to approximately -18 °C over the following week as the warm AR layer collapsed (Fig. 4a). IWV dropped below 1.2 kg m⁻² on 24 March – among the lowest March values observed in the long-term record (Maturilli, 2022) – and remained below 4 kg m⁻² thereafter (Fig. 4b). This column drying coincided with rising 230 vapour d-excess (Fig. 4a), consistent with establishment of a cold, dry Arctic air mass during the CAO.

3.3 Surface observations at Ny-Ålesund

The AR began influencing western Svalbard on 12 March 2022, triggering a sustained perturbation of near-surface atmospheric conditions (Fig. 5). Water vapour mixing ratios rose above winter baseline levels and remained elevated (>4,000 ppmv) for ~120 hours (12 March 16:30 to 17 March 15:00). As the AR made landfall on 15 March, mixing ratios tripled from a winter 235 baseline of 2,304 ppmv to a peak of 6,690 ppmv, marking the arrival of the exceptionally humid air mass (Fig. 5a).

Water vapor isotopes responded simultaneously: δ¹⁸O increased by +8.8 ‰ and δ²H by +56.1 ‰ relative to the winter baseline, reaching campaign maxima on 15 March (-14.2 ‰ and -113.4 ‰, respectively; Fig. 5b and Supplementary Fig. S1). In contrast, d-excess decreased steadily from 12 March, reaching a campaign minimum of -10.5 ‰ on 16 March (Fig. 3c). Snowfall isotope 240 samples from Ny-Ålesund broadly track the water vapour variability, with snowfall δ¹⁸O and d-excess averaging ~11 ‰ higher than vapour, consistent with equilibrium condensation fractionation (Supplementary Table S1). Sodium aerosol (Na⁺) concentrations also increased sharply as the AR made landfall, rising from background values (~0.01 μg m⁻³) to 1.8 μg m⁻³ on 15-16 March (Fig. 5d).



245

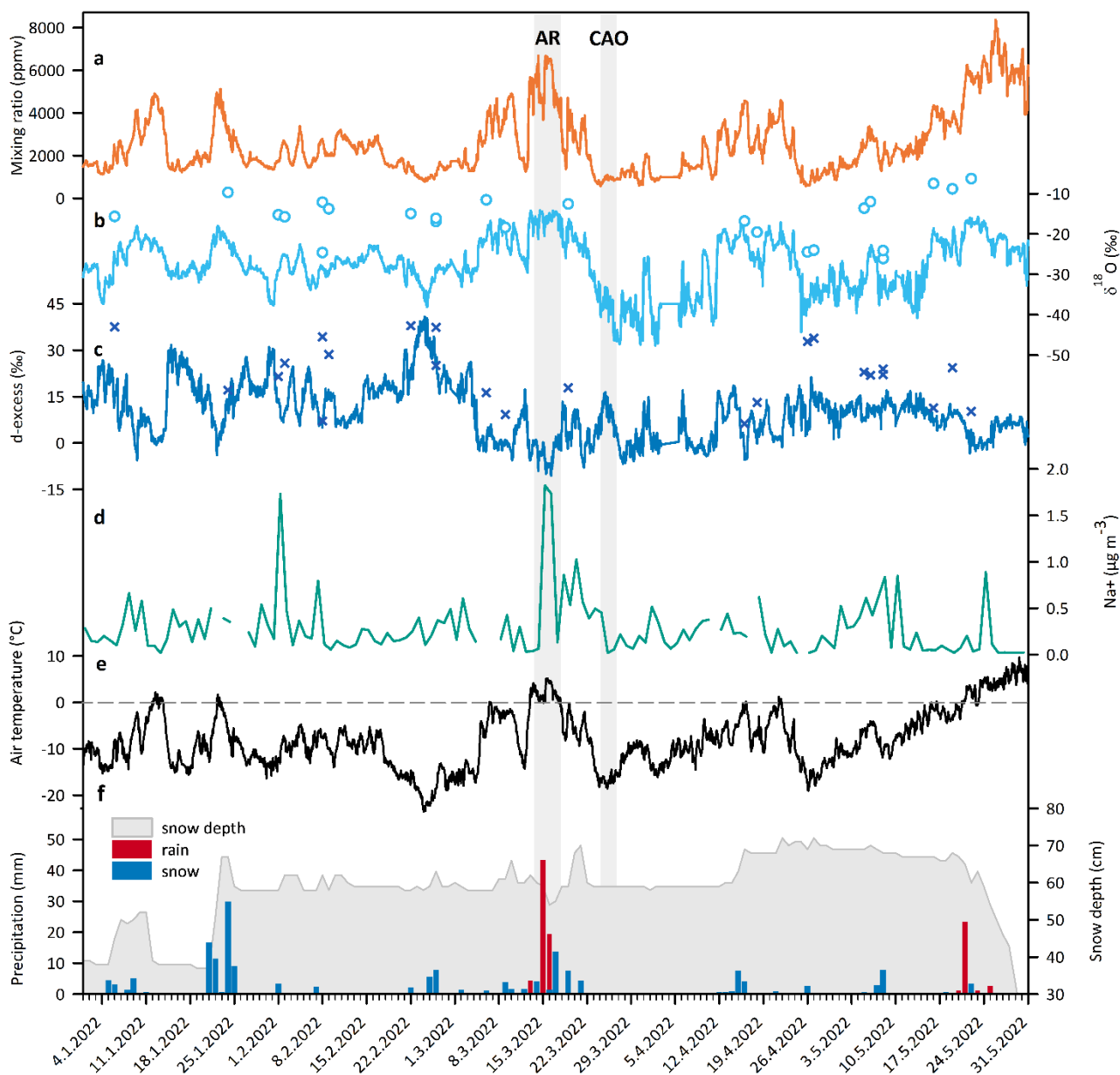


Figure 5: Observations at Ny-Ålesund during winter–spring 2022. Water vapour (a) mixing ratio, (b) $\delta^{18}\text{O}$, (c) d-excess, and (d) sodium (Na^+) aerosol concentration measured at the Zeppelin Observatory; (e) 2-m air temperature, (f) snow depth (grey shading) and daily precipitation amount and phase (rain: red; snow: blue)(Champagne et al., 2024) from the Ny-Ålesund meteorological station (SN99910). Discrete snowfall isotope samples collected in Ny-Ålesund are shown as circles ($\delta^{18}\text{O}$) and crosses (d-excess) in (b) and (c), respectively. The mid-March AR and subsequent CAO are indicated by grey vertical shading.

250



255 These atmospheric anomalies were accompanied by pronounced surface meteorological changes. Daily mean 2m air temperatures rose rapidly above freezing, reaching a record March maximum of 5.6 °C on 15 March, coincident with intense rainfall (Fig. 5e, f). A total of 43.9 mm of rain fell that day – the highest daily March rainfall at Ny-Ålesund since observations began in 1975 (Champagne et al., 2024). Snow depth decreased by ~50 mm, consistent with rainfall-driven compaction and partial melt of the pre-existing snowpack (Fig. 5f).

260 Following the AR, conditions evolved toward a cold and dry regime characteristic of a CAO (Fig. 1b). From 21 March onward, mixing ratios declined below 1,000 ppmv, while vapour $\delta^{18}\text{O}$ and $\delta^2\text{H}$ reached campaign minima on 26 March (~-47.5 ‰ and -380 ‰; Fig. 3a,b). Over the same period, d-excess increased by ~27 ‰ relative to AR conditions (Fig. 5a–c). This transition coincided with a reversal in large-scale flow associated with cyclonic activity east of Svalbard, enhancing northerly advection of cold Arctic air across the Fram Strait (Fig. 1b). SATs fell below -18 °C and Na^+ concentrations returned to near-zero levels (Fig. 3d–f). Snowfall was confined to the period immediately following the AR, with none observed during the subsequent
265 CAO (Fig. 5f).

3.3 Precipitation phase and surface energy response

270 Rain-snow partitioning during the AR was governed by rapid changes in the melting level – the height at which falling snow begins to melt – derived from radiosonde wet-bulb temperature profiles (Supplementary Fig. S2). The melting level rose from ~100–350 m a.s.l. during the early AR phase to 585 m a.s.l. on 15 March, before collapsing to ~22 m a.s.l. on 16 March as the warm maritime column broke down. This evolution closely tracked the transition from mixed-phase precipitation to rainfall and back to snowfall at Ny-Ålesund (Champagne et al., 2024) (Fig. 5f). Meteorological station observations further document the AR's progression across Svalbard, with rainfall first recorded at Hornsund and Ny-Ålesund (Fig. 6a). Peak totals occurred at Ny-Ålesund on 15 March, exceeding those at other stations by more than fivefold (Fig. 6c).

275 Across Svalbard, ERA5 fields (Hersbach et al., 2020) for 15–16 March 2022 reveal pronounced spatial variability in precipitation magnitude and phase (Fig. 6). The AR delivered ~0.7 Gt of precipitation in total, comprising ~0.5 Gt snowfall and ~0.2 Gt rainfall (Fig. 5a–b). Although rainfall accounted for less than one-third of the total, it extended across nearly two-thirds of glacierised terrain, primarily along western coastal margins (Fig. 6a). Snowfall was concentrated over high terrain, with mean accumulations of 30.4, 6.7 and 5.2 mm w.e. across the NW, NE and S glacier regions, respectively, and peak totals
280 exceeding 40 mm w.e. in the NW (Fig. 6b). Over the Holtedahlfonna–Kronebreen glacier system (385 km²; 0–1,441 m a.s.l.), for which seasonal mass balance data are available (WGMS, 2025), the AR delivered 42.3 mm w.e. of snowfall – equivalent to 8.3 % of the 2022 winter accumulation, offsetting its annual net mass deficit (excluding calving) by ~5 %.

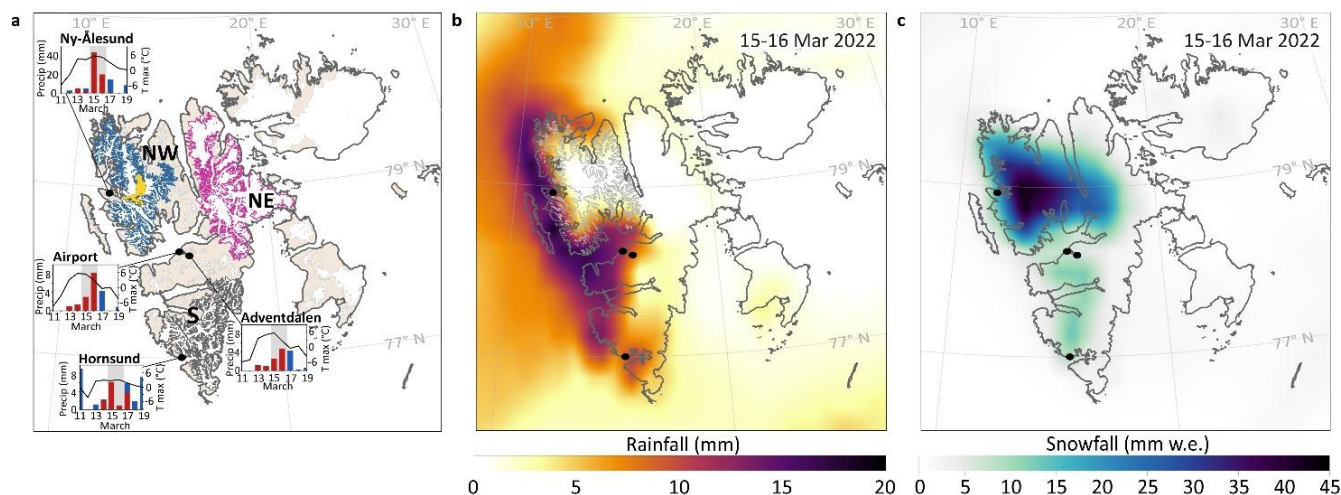


Figure 6: March 2022 AR rain-snow partitioning. (a) Observed daily precipitation amount, phase (red: rain, blue: snow), and maximum air temperatures (Tmax) for 11-19 March 2022 recorded at select meteorological stations (black circles) (Norwegian Centre for Climate Services, 2022). Grey vertical shading denotes peak AR conditions. Glacier regions on Spitsbergen are indicated (NW, NE, S), with the Holtedahlfonna-Kronebreen glacier system highlighted in yellow (RGI 7.0 Consortium, 2023). Total ERA5 (b) rainfall and (c) snowfall between 15-16 March 2022 (Hersbach et al., 2020). The grey 585 m contour in (b) marks the radiosonde-derived melting level during the AR. Black circles indicate meteorological stations in (a). Basemaps from the Norwegian Polar Institute (2014).

285

ERA5 data further show that the AR substantially perturbed atmospheric forcing and components of the surface energy budget across Svalbard (Fig. 7). Relative to the 1981–2010 March baseline (Hersbach et al., 2020), IWV increased by up to 8 mm along the west coast (Fig. 7a), reaching absolute values of ~13 mm on 15 March – approximately four-fold above the long-term March mean. This anomalous moisture loading enhanced atmospheric emissivity, with downward longwave radiation exceeding baseline values by $>100 \text{ W m}^{-2}$ across northwestern Svalbard (Fig. 7b). Total precipitation anomalies reached up to 40 mm, concentrated over high terrain in the NW glacier region and around Ny-Ålesund (Fig. 7c).

295

Surface thermodynamic anomalies were strongly elevation-dependent. Skin temperature anomalies reached $+6 \text{ }^\circ\text{C}$ at Ny-Ålesund and up to $+20 \text{ }^\circ\text{C}$ over Holtedahlfonna and parts of the NE region (Fig. 7d). Turbulent exchange intensified, with latent heat flux anomalies up to $\sim 60 \text{ W m}^{-2}$ along the western coastal margin, decreasing with elevation (Fig. 7e). Despite these pronounced atmospheric and surface perturbations, snowmelt remained largely confined to low-elevation western coastal zones and across the south, rising to 28 mm (over the 2-day period) in west-central Spitsbergen and $\sim 6 \text{ mm}$ around Ny-Ålesund. Snow surfaces above $\sim 500 \text{ m a.s.l.}$ exhibited no detectable snow melt response (Fig. 7f). In total, net snowmelt across Svalbard was $\sim 0.04 \text{ Gt}$ between 15-16 March, 62% of which impacted glaciers, with the remainder affecting seasonally snow-covered but ice-free terrain.

305

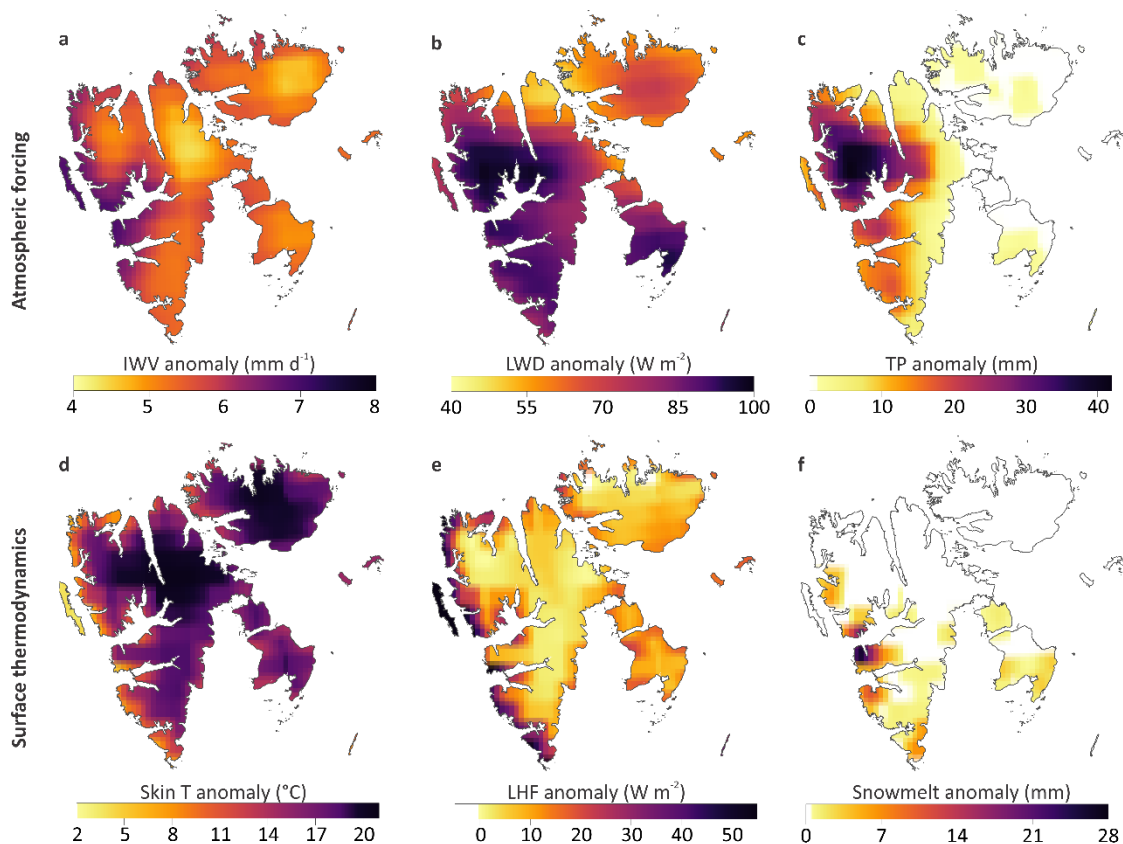


Figure 7: Atmospheric and surface anomalies during the March 2022 AR. Spatial distribution of (a) mean integrated water vapour (IWV), (b) mean downward longwave radiation (LWD), (c) total precipitation (TP), (d) mean skin temperature (T), (e) mean latent heat flux (LHF; positive downward), and (f) total snowmelt anomalies on 15–16 March 2022, relative to the 1981–2010 March baseline (Hersbach et al., 2020).

310

4. Discussion

The March 2022 AR ranks among the most intense winter atmospheric intrusions observed in the High Arctic (Ebell et al., 2025). The 43.9 mm of liquid precipitation recorded at Ny-Ålesund in a single day represents a fourfold increase of the upper-decile AR-associated total (10 mm; 2017–2021) and is nearly an order of magnitude greater than the median winter AR rainfall (5 mm), placing this event at the extreme end of documented Svalbard ARs.

315

Such exceptional winter rainfall requires not only anomalous moisture flux but sustained poleward transport that retains high column humidity. Our vapour isotope record captures distinct pulses of Atlantic moisture marked by elevated $\delta^{18}\text{O}$, negative d-excess, and a near-meteoric slope, indicating high-humidity marine evaporation and – crucially – limited progressive rainout during poleward transport (Bailey et al., 2021; Bonne et al., 2015; Leroy-Dos Santos et al., 2020). The concurrent spike in

320



marine Na⁺ aerosol further supports direct Atlantic influence and minimal upstream wet scavenging of sea-salt aerosols during transport (Yamagata et al., 2009). In contrast, the March CAO exhibits a depleted isotopic end-member and shallower slope, reflecting stronger kinetic fractionation during air-mass transformation across the sea ice–open water boundary in the Fram Strait under cold, lower-humidity conditions (Brunello et al., 2023; Mix et al., 2019). Cross sections show a low-level jet
325 transporting a deep moisture plume toward Svalbard, with cloud liquid water concentrated below ~2-3 km and depleted only in the lee of the NW glaciated region through orographic precipitation. Together, these observations indicate that the March 2022 AR delivered a moisture-rich Atlantic air mass to Svalbard with minimal depletion during transport, maintaining high atmospheric humidity and priming the surface for strong radiative forcing.

330 This atmospheric perturbation reorganised Svalbard’s winter surface energy balance through three reinforcing mechanisms. First, enhanced I WV increased atmospheric emissivity, driving a strong rise in downward longwave radiation that dominated net energy input while shortwave forcing remained minimal at this latitude in late winter. Second, near-saturated AR conditions generated positive latent heat flux anomalies, enhancing downward transfer of latent energy and augmenting longwave-driven warming. Third, rapid elevation of the melting level redistributed this energy vertically across the glacier system, exposing
335 low-elevation snowpacks to rainfall while warming higher-elevation surfaces. Cross-sectional temperature structure confirms a shallow warm maritime layer confined to the lowest ~700-900 m, intersecting the peak of Svalbard’s glacier hypsometry (~450 m a.s.l.) while the highest ice caps remained below freezing. Skin temperature responded rapidly, with anomalies reaching up to +20 °C over the NW glacierised region. Together, these coupled perturbations eroded the winter thermal deficit and drove significant snowmelt despite the event’s winter timing (Fig. 7).

340 The AR generated a mean daily snowmelt of 0.45 mm d⁻¹ across Svalbard, exceeding the long-term March climatology (0.001 mm d⁻¹) by more than two orders of magnitude. Simultaneously, ~60 % of Svalbard’s glacierised area received ≥1 mm of rainfall. Yet independent snow pit observations at Ny-Ålesund show that local snow water equivalent increased (Salzano et al., 2023), demonstrating that much of the liquid input was retained within the snowpack. Where water entered this cold late-
345 winter snowpack, percolation and refreezing would densify near-surface layers and form internal ice horizons (Mikkelsen et al., 2016), releasing latent heat and modifying snowpack thermal structure, thereby contributing to firn densification (Möller and Kohler, 2018; Van Pelt et al., 2016; Van Pelt and Kohler, 2015). This interpretation is consistent with the observed ~50 mm reduction in snowpack depth (Fig. 5), indicative of compaction, densification and internal refreezing rather than substantial meltwater runoff. Ice layers documented in the snow stratigraphy of nearby Austre Lovénbreen (~8 km southwest
350 of Ny-Ålesund) further support the occurrence of local melt and refreezing processes across low-elevation glacier surfaces (Bernard and Friedt, 2025). Notably, the same study reports earlier seasonal ice exposure relative to 2023, demonstrating that winter ROS episodes can precondition glacier surfaces for earlier ablation onset despite short-term liquid retention. Although much of this liquid input was temporarily retained within the snowpack, the ~0.2 Gt of rainfall and ~0.04 Gt of snowmelt nonetheless pre-loaded the hydrological system, storing freshwater with the potential to influence runoff timing and magnitude
355 during the subsequent melt season (Kleber et al., 2025).



Across the archipelago, accumulation dominated the mass response: the 0.5 Gt of AR-fuelled snowfall represents ~3–4% of Svalbard’s mean annual total ice mass loss (Sasgen et al., 2024) and ~7% of its surface mass balance deficit (Schuler et al., 2020). These results demonstrate that a single late-winter AR can deliver sufficient snowfall over a two-day period to offset a measurable fraction of the annual net mass loss, consistent with observations in Greenland and Antarctica (Bailey and Hubbard, 2025; Gorodetskaya et al., 2014). Yet this event was not merely exceptional in magnitude, but dynamically efficient with a strong but nuanced impact on glacier mass balance (Hubbard et al., 2000). The rapid elevations of the melting level by several hundred metres tipped ~60% of Svalbard’s glacierised area across the winter snow-rain threshold. Although the March 2022 AR demonstrates the capacity of seasonal snow and firn to buffer substantial liquid input through refreezing and internal storage – with refreezing contributing ~34% of Svalbard’s mass gain (Möller and Kohler, 2018) – these processes depend critically on snowpack thickness, density profile, and thermal state. Moreover, Svalbard’s glacier hypsometry peaks at ~450 m a.s.l (Noël et al., 2020), just below the melting level reached during the AR, meaning that even modest thermodynamic shifts in melt-elevation will redistribute precipitation phase across a disproportionately large area of the glacierised surface.

5. Conclusions

Since 1979, winter IVT into this Atlantic sector of the Arctic has increased (Rinke et al., 2019), and projections indicate continued intensification and increasing frequency of winter ARs (Nellikkattil et al., 2023; Thaker et al., 2025). In a sensitive maritime Arctic climate increasingly poised near 0 °C, stronger ARs will shift winter precipitation from snow to rainfall (Bintanja and Andry, 2017), reducing the buffering role of snow and firn (Möller and Kohler, 2018) and accelerating Svalbard’s runoff and glacier mass loss to proglacial and marine systems (Kopec et al., 2024). These phase transitions also destabilise snowpack structure (Hansen et al., 2019; Sobota et al., 2020; Vickers et al., 2025) and tundra ecosystems (Aalto et al., 2026; Hiltunen et al., 2022; Niittynen et al., 2020), amplifying ROS hazards (Eckerstorfer and Christiansen, 2012). Svalbard therefore provides a natural testbed for AR-driven winter climate transitions in a rapidly warming Arctic, with the March 2022 event offering a process-level analogue for how continued Arctic amplification is shifting high-latitude winters toward increasingly rain-dominated extremes – despite their capacity to episodically replenish glacier mass.

380 Data availability

Atmospheric water vapour isotope data are available in the Supporting Information (Dataset 1), and under a Creative Commons Attribution 4.0 International license at <https://doi.org/10.5281/zenodo.18888750>. Ny-Ålesund radiosonde measurements are available at <https://doi.pangaea.de/10.1594/PANGAEA.944406>. Surface meteorological observations from Svalbard stations are available at <https://seklima.met.no/>. Sodium aerosol data measured at the Zeppelin Observatory are provided by NILU at <https://ebas.nilu.no/>. Integrated vapour transport (IVT) data are available at <https://www.frdr-dfdr.ca/repo/dataset/b1798e59-b38e-4a83-ab88-12d0a8aca28f>. Glacier mass balance data are available through the World Glacier Monitoring Service at



<https://wgms.ch/latest-glacier-mass-balance-data/>. Glacier outlines are provided by the Randolph Glacier Inventory at <https://www.glims.org/RGI/>. ERA5 and CARRA data are available from the Copernicus Climate Data Store at <https://cds.climate.copernicus.eu>. MODIS Satellite images are available at <https://www.earthdata.nasa.gov/>. Svalbard basemaps are available from the Norwegian Polar Institute at <https://data.npolar.no/dataset/44ca8c2a-22c2-49e8-a50b-972734f287e3>. The base maps in Figure 2 derive from the ETOPO5 gridded data set available at NOAA National Centers for Environmental Information here <https://doi.org/10.25921/fd45-gt74>.

Author contributions

Conceptualisation: HB and AH. Methodology: HB, JEB, BGK, VH, JMW, DVD, and AH. Formal analysis: HB and JEB. Investigation: HB, JEB, BGK, VH, JK, DVD and AH. Resources: HB, JMW, HM, DVD and AH. Data Curation: HB, BGK, VH, JK, and DVD. Writing - Original Draft: HB. Writing - Review & Editing: HB, AH, JEB, JMW, and HM. Visualisation: HB and JEB. Funding acquisition: HB, JMW, and AH. Project administration: HB.

Competing interests

The authors declare no competing interests.

Disclaimer

Copernicus Publications remains neutral with regard to jurisdictional claims made in the text, published maps, institutional affiliations, or any other geographical representation in this paper. While Copernicus Publications makes every effort to include appropriate place names, the final responsibility lies with the authors. Views expressed in the text are those of the authors and do not necessarily reflect the views of the publisher.”

Acknowledgements

This study was funded by a Research Council of Finland grant to HB (348536) and the Water, Energy and Environmental Engineering Research Unit at the University of Oulu. This work contributes to the Research Council of Finland-funded Digital Waters (DIWA) Flagship. Water vapour isotope measurements were supported by the UArctic Chair positions held by JMW and AH, and by the University of Oulu and UiT – The Arctic University of Norway. JEB and CARRA project has been supported by EU C3S 2017/C3S_322_Lot2_METNO/SC2 and C3S2_361a contracts. AH gratefully acknowledges support through a UArctic Chair in Cryospheric Science, the Research Council of Norway (AFG 342265), Research Council of Finland (Grant 363970) and the Otto Malm Foundation (Grant 13678). We thank personnel of Ny-Ålesund Research Station – Sverdrup for assistance with collecting fresh snow samples, and the FARLAB at the University of Bergen for their isotopic analysis. We



415 also thank staff at the Zeppelin Observatory for maintaining the vapour isotope instrumentation and supporting long-term atmospheric observations.

Financial support

Support funds and grant agreement numbers are listed as specified upon manuscript registration and reported to FundRef upon publication.

420 References

- Aalto, J., Kämäräinen, M., Rantanen, M., Niittynen, P., Phoenix, G. K., Lenoir, J., Maclean, I., and Luoto, M.: A new era of bioclimatic extremes in the terrestrial Arctic, *Sci. Adv.*, 12, eadw5698, <https://doi.org/10.1126/sciadv.adw5698>, 2026.
- Adusumilli, S., A. Fish, M., Fricker, H. A., and Medley, B.: Atmospheric River Precipitation Contributed to Rapid Increases in Surface Height of the West Antarctic Ice Sheet in 2019, *Geophys. Res. Lett.*, 48, <https://doi.org/10.1029/2020GL091076>,
425 2021.
- Akers, P. D., Kopec, B. G., Klein, E. S., Bailey, H., and Welker, J. M.: The Pivotal Role of Evaporation in Lake Water Isotopic Variability Across Space and Time in a High Arctic Periglacial Landscape, *Water Resour. Res.*, 60, e2023WR036121, <https://doi.org/10.1029/2023WR036121>, 2024.
- Ala-Aho, P., Welker, J. M., Bailey, H., Pedersen, S. H., Kopec, B., Klein, E., Mellat, M., Mustonen, K.-R., Noor, K., and
430 Marttila, H.: Arctic snow isotope hydrology: A comparative snow-water vapor study, *Atmosphere (Basel)*, 12, <https://doi.org/10.3390/atmos12020150>, 2021.
- Bailey, H. and Hubbard, A.: Snow Mass Recharge of the Greenland Ice Sheet Fueled by Intense Atmospheric River, *Geophys. Res. Lett.*, 52, e2024GL110121, <https://doi.org/10.1029/2024GL110121>;PAGEGROUP:STRING:PUBLICATION, 2025.
- Bailey, H., Hubbard, A., Klein, E. S., Mustonen, K. R., Akers, P. D., Marttila, H., and Welker, J. M.: Arctic sea-ice loss fuels
435 extreme European snowfall, *Nat. Geosci.*, 14, 283–288, <https://doi.org/10.1038/S41561-021-00719-Y>, 2021.
- Bailey, H. L., Kaufman, D. S., Sloane, H. J., Hubbard, A. L., Henderson, A. C. G., Leng, M. J., Meyer, H., and Welker, J. M.: Holocene atmospheric circulation in the central North Pacific: A new terrestrial diatom and $\delta^{18}\text{O}$ dataset from the Aleutian Islands, *Quat. Sci. Rev.*, 194, <https://doi.org/10.1016/j.quascirev.2018.06.027>, 2018.
- Bernard, É. and Friedt, J. M.: Did a global heatwave have a lasting impact on the snowpack and the annual glacier mass
440 balance? The example of a small glacial basin observatory in the High Arctic (Brøgger Peninsula, Spitsbergen), *Arct. Antarct. Alp. Res.*, 57, <https://doi.org/10.1080/15230430.2025.2479899>, 2025.
- Bintanja, R. and Andry, O.: Towards a rain-dominated Arctic, *Nature Climate Change* 2017 7:4, 7, 263–267, <https://doi.org/10.1038/nclimate3240>, 2017.



- Bonne, J.-L., Steen-Larsen, H. C., Risi, C., Werner, M., Sodemann, H., Lacour, J.-L., Fettweis, X., Cesana, G., Delmotte, M.,
445 Cattani, O., Vallelonga, P., Kjaer, H. A., Clerbaux, C., Sveinbjörnsdóttir, Á. E., and Masson-Delmotte, V.: The summer 2012
Greenland heat wave: In situ and remote sensing observations of water vapor isotopic composition during an atmospheric river
event, *Journal of Geophysical Research: Atmospheres*, 120, 2970–2989, <https://doi.org/10.1002/2014JD022602>, 2015.
- Box, J. E., Wehrlé, A., van As, D., Fausto, R. S., Kjeldsen, K. K., Dachauer, A., Ahlstrøm, A. P., and Picard, G.: Greenland
Ice Sheet Rainfall, Heat and Albedo Feedback Impacts From the Mid-August 2021 Atmospheric River, *Geophys. Res. Lett.*,
450 49, <https://doi.org/10.1029/2021GL097356>, 2022.
- Box, J. E., Nielsen, K. P., Yang, X., Niwano, M., Wehrlé, A., van As, D., Fettweis, X., Køltzow, M. A. Ø., Palmason, B.,
Fausto, R. S., van den Broeke, M. R., Huai, B., Ahlstrøm, A. P., Langley, K., Dachauer, A., and Noël, B.: Greenland ice sheet
rainfall climatology, extremes and atmospheric river rapids, *Meteorological Applications*, 30, e2134,
<https://doi.org/10.1002/met.2134>, 2023.
- 455 Brunello, C. F., Meyer, H., Mellat, M., Casado, M., Bucci, S., Dütsch, M., and Werner, M.: Contrasting Seasonal Isotopic
Signatures of Near-Surface Atmospheric Water Vapor in the Central Arctic During the MOSAiC Campaign, *Journal of
Geophysical Research: Atmospheres*, 128, e2022JD038400, <https://doi.org/10.1029/2022JD038400>, 2023.
- Champagne, O., Zolina, O., Dedieu, J.-P., Wolff, M., and Jacobi, H.-W.: Artificial Trends or Real Changes? Investigating
Precipitation Records in Ny-Ålesund, Svalbard, *J. Hydrometeorol.*, 25, 809–825, <https://doi.org/10.1175/JHM-D-23-0182.1>,
460 2024.
- Croghan, D., Pedron, S. A., Redman, Z. C., Kopec, B. G., Klein, E. S., Hubbard, A., Tomco, P. L., Feldman, G. C., Czimczik,
C. I., and Welker, J. M.: Western Greenland Ice Sheet-Land-Ocean Interactions: Near-Shore Dissolved Organic Carbon 14C
Ages and Composition in Eastern Baffin Bay, *J. Geophys. Res. Biogeosci.*, 130, e2024JG008705,
<https://doi.org/10.1029/2024JG008705>, 2025.
- 465 Davies-Jones, R.: An Efficient and Accurate Method for Computing the Wet-Bulb Temperature along Pseudoadiabats, *Mon.
Weather Rev.*, 136, 2764–2785, <https://doi.org/10.1175/2007MWR2224.1>, 2008.
- Ebell, K., Buhren, C., Gierens, R., Chellini, G., Lauer, M., Walbröl, A., Dahlke, S., Krobot, P., and Mech, M.: Impact of
weather systems on observed precipitation at Ny-Ålesund (Svalbard), *Atmos. Chem. Phys.*, 25, 7315–7342,
<https://doi.org/10.5194/ACP-25-7315-2025>, 2025.
- 470 Eckerstorfer, M. and Christiansen, H. H.: Meteorology, Topography and Snowpack Conditions causing Two Extreme Mid-
Winter Slush and Wet Slab Avalanche Periods in High Arctic Maritime Svalbard, *Permafr. Periglac. Process.*, 23, 15–25,
<https://doi.org/10.1002/ppp.734>, 2012.
- Freitas, G. P., Kopec, B., Adachi, K., Krejci, R., Heslin-Rees, D., Yttri, K. E., Hubbard, A., Welker, J. M., and Zieger, P.:
Contribution of fluorescent primary biological aerosol particles to low-level Arctic cloud residuals, *Atmos. Chem. Phys.*, 24,
475 5479–5494, <https://doi.org/10.5194/acp-24-5479-2024>, 2024.
- Geyman, E. C., J. J. van Pelt, W., Maloof, A. C., Aas, H. F., and Kohler, J.: Historical glacier change on Svalbard predicts
doubling of mass loss by 2100, *Nature* 2022 601:7893, 601, 374–379, <https://doi.org/10.1038/s41586-021-04314-4>, 2022.



- Gorodetskaya, I. V., Tsukernik, M., Claes, K., Ralph, M. F., Neff, W. D., and Van Lipzig, N. P. M.: The role of atmospheric rivers in anomalous snow accumulation in East Antarctica, *Geophys. Res. Lett.*, 41, 6199–6206, 480 <https://doi.org/10.1002/2014GL060881>, 2014.
- Gorodetskaya, I. V., Durán-Alarcón, C., González-Herrero, S., Clem, K. R., Zou, X., Rowe, P., Rodriguez Imazio, P., Campos, D., Leroy-Dos Santos, C., Dutrievoz, N., Wille, J. D., Chyhareva, A., Favier, V., Blanchet, J., Pohl, B., Cordero, R. R., Park, S.-J., Colwell, S., Lazzara, M. A., Carrasco, J., Gulisano, A. M., Krakovska, S., Ralph, F. M., Dethinne, T., and Picard, G.: Record-high Antarctic Peninsula temperatures and surface melt in February 2022: a compound event with an intense 485 atmospheric river, *NPJ Clim. Atmos. Sci.*, 6, <https://doi.org/10.1038/s41612-023-00529-6>, 2023.
- Hansen, B. B., Lorentzen, J. R., Welker, J. M., Varpe, Ø., Aanes, R., Beumer, L. T., and Pedersen, Å. Ø.: Reindeer turning maritime: Ice-locked tundra triggers changes in dietary niche utilization, *Ecosphere*, 10, e02672, <https://doi.org/10.1002/ECS2.2672>;REQUESTEDJOURNAL:JOURNAL:21508925;WGROU:STRING:PUBLICATION, 2019.
- 490 Hegyi, B. M. and Taylor, P. C.: The Unprecedented 2016–2017 Arctic Sea Ice Growth Season: The Crucial Role of Atmospheric Rivers and Longwave Fluxes, *Geophys. Res. Lett.*, 45, 5204–5212, <https://doi.org/10.1029/2017GL076717>;CTYPE:STRING:JOURNAL, 2018.
- Hersbach, H., Bell, B., Berrisford, P., Hirahara, S., Horányi, A., Muñoz-Sabater, J., Nicolas, J., Peubey, C., Radu, R., Schepers, D., Simmons, A., Soci, C., Abdalla, S., Abellan, X., Balsamo, G., Bechtold, P., Biavati, G., Bidlot, J., Bonavita, M., De Chiara, 495 G., Dahlgren, P., Dee, D., Diamantakis, M., Dragani, R., Flemming, J., Forbes, R., Fuentes, M., Geer, A., Haimberger, L., Healy, S., Hogan, R. J., Hólm, E., Janisková, M., Keeley, S., Laloyaux, P., Lopez, P., Lupu, C., Radnoti, G., de Rosnay, P., Rozum, I., Vamborg, F., Villaume, S., and Thépaut, J. N.: The ERA5 global reanalysis, *Quarterly Journal of the Royal Meteorological Society*, <https://doi.org/10.1002/qj.3803>, 2020.
- Hiltunen, T. A., Stien, A., Väisänen, M., Ropstad, E., Aspi, J. O., and Welker, J. M.: Svalbard reindeer winter diets: Long- 500 term dietary shifts to graminoids in response to a changing climate, *Glob. Chang. Biol.*, 28, 7009–7022, <https://doi.org/10.1111/GCB.16420>;PAGEGROUP:STRING:PUBLICATION, 2022.
- Hubbard, A., Willis, I., Sharp, M., Mair, D., Nienow, P., Hubbard, B., and Blatter, H.: Glacier mass-balance determination by remote sensing and high-resolution modelling, *Journal of Glaciology*, 46, 491–498, <https://doi.org/10.3189/172756500781833016>, 2000.
- 505 Kirbus, B., Schirmacher, I., Klingebiel, M., Schäfer, M., Ehrlich, A., Slättberg, N., Lucke, J., Moser, M., Müller, H., and Wendisch, M.: Thermodynamic and cloud evolution in a cold-air outbreak during HALO-(AC)³: quasi-Lagrangian observations compared to the ERA5 and CARRA reanalyses, *Atmos. Chem. Phys.*, 24, 3883–3904, <https://doi.org/10.5194/ACP-24-3883-2024>.
- Kleber, G. E., Magerl, L., Turchyn, A. V., Schloemer, S., Trimmer, M., Zhu, Y., and Hodson, A.: Proglacial methane emissions 510 driven by meltwater and groundwater flushing in a high-Arctic glacial catchment, *Biogeosciences*, 22, 659–674, <https://doi.org/10.5194/bg-22-659-2025>, 2025.



- Kopec, B. G., Klein, E. S., Feldman, G. C., Pedron, S. A., Bailey, H., Causey, D., Hubbard, A., Marttila, H., and Welker, J. M.: Arctic Freshwater Sources and Ocean Mixing Relationships Revealed With Seawater Isotopic Tracing, *J. Geophys. Res. Oceans*, 129, e2023JC020583, <https://doi.org/10.1029/2023JC020583>, 2024.
- 515 Lapointe, F., Karmalkar, A. V., Bradley, R. S., Retelle, M. J., and Wang, F.: Climate extremes in Svalbard over the last two millennia are linked to atmospheric blocking, *Nature Communications* 2024 15:1, 15, 4432-, <https://doi.org/10.1038/s41467-024-48603-8>, 2024.
- Leroy-Dos Santos, C., Masson-Delmotte, V., Casado, M., Fourré, E., Steen-Larsen, H. C., Maturilli, M., Orsi, A., Berchet, A., Cattani, O., Minster, B., Gherardi, J., and Landais, A.: A 4.5 Year-Long Record of Svalbard Water Vapor Isotopic Composition Documents Winter Air Mass Origin, *Journal of Geophysical Research: Atmospheres*, 125, e2020JD032681, <https://doi.org/10.1029/2020JD032681>, 2020.
- 520 Maclennan, M. L., Lenaerts, J. T. M., Shields, C., and Wille, J. D.: Contribution of Atmospheric Rivers to Antarctic Precipitation, *Geophys. Res. Lett.*, 49, <https://doi.org/10.1029/2022GL100585>, 2022.
- Madsen, M. V., Steen-Larsen, H. C., Hörhold, M., Box, J., Berben, S. M. P., Capron, E., Faber, A. -K., Hubbard, A., Jensen, 525 M. F., Jones, T. R., Kipfstuhl, S., Koldtoft, I., Pillar, H. R., Vaughn, B. H., Vladimirova, D., and Dahl-Jensen, D.: Evidence of Isotopic Fractionation During Vapor Exchange Between the Atmosphere and the Snow Surface in Greenland, *Journal of Geophysical Research: Atmospheres*, 124, 2932–2945, <https://doi.org/10.1029/2018JD029619>, 2019.
- Mattingly, K. S., Mote, T. L., and Fettweis, X.: Atmospheric River Impacts on Greenland Ice Sheet Surface Mass Balance, *Journal of Geophysical Research: Atmospheres*, 123, 8538–8560, <https://doi.org/10.1029/2018JD028714>, 2018.
- 530 Mattingly, K. S., Mote, T. L., Fettweis, X., As, D. V. A. N., Tricht, K. V. A. N., Lhermitte, S., Pettersen, C., and Fausto, R. S.: Strong Summer Atmospheric Rivers Trigger Greenland Ice Sheet Melt through Spatially Varying Surface Energy Balance and Cloud Regimes, *J. Clim.*, 33, 6809–6832, <https://doi.org/10.1175/JCLI-D-19-0835.1>, 2020.
- Mattingly, K. S., Turton, J. V., Wille, J. D., Noël, B., Fettweis, X., Rennermalm, Å. K., and Mote, T. L.: Increasing extreme melt in northeast Greenland linked to foehn winds and atmospheric rivers, *Nat. Commun.*, 14, <https://doi.org/10.1038/s41467-023-37434-8>, 2023.
- 535 Maturilli, M.: High resolution radiosonde measurements from station Ny-Ålesund (2022-03), <https://doi.org/doi.org/10.1594/PANGAEA.914973>, 2022.
- Mellat, M., Bailey, H., Mustonen, K. R., Marttila, H., Klein, E. S., Gribanov, K., Bret-Harte, M. S., Chupakov, A. V., Divine, D. V., Else, B., Filippov, I., Hyöky, V., Jones, S., Kirpotin, S. N., Kroon, A., Markussen, H. T., Nielsen, M., Olsen, M., 540 Paavola, R., Pokrovsky, O. S., Prokushkin, A., Rasch, M., Raundrup, K., Suominen, O., Syvänperä, I., Vignisson, S. R., Zarov, E., and Welker, J. M.: Hydroclimatic Controls on the Isotopic ($\delta^{18}\text{O}$, $\delta^2\text{H}$, d-excess) Traits of Pan-Arctic Summer Rainfall Events, *Front. Earth Sci. (Lausanne)*, 9, 367, <https://doi.org/10.3389/FEART.2021.651731/BIBTEX>, 2021.
- Mikkelsen, A. B., Hubbard, A., Macferrin, M., Eric Box, J., Doyle, S. H., Fitzpatrick, A., Hasholt, B., Bailey, H. L., Lindbäck, K., and Pettersson, R.: Extraordinary runoff from the Greenland ice sheet in 2012 amplified by hypsometry and depleted firn 545 retention, *Cryosphere*, 10, <https://doi.org/10.5194/tc-10-1147-2016>, 2016.



- Mix, H. T., Reilly, S. P., Martin, A., and Cornwell, G.: Evaluating the Roles of Rainout and Post-Condensation Processes in a Landfalling Atmospheric River with Stable Isotopes in Precipitation and Water Vapor, *Atmosphere* 2019, Vol. 10, 10, <https://doi.org/10.3390/ATMOS10020086>, 2019.
- Mo, R.: EDARA: An ERA5-based Dataset for Atmospheric River Analysis, *Scientific Data* 2024 11:1, 11, 900-,
550 <https://doi.org/10.1038/s41597-024-03679-1>, 2024.
- Möller, M. and Kohler, J.: Differing Climatic Mass Balance Evolution Across Svalbard Glacier Regions Over 1900–2010, *Front. Earth Sci. (Lausanne)*, 6, 369364, <https://doi.org/10.3389/feart.2018.00128>, 2018.
- Nellikattil, A. B., Lee, J. Y., Guan, B., Timmermann, A., Lee, S. S., Chu, J. E., and Lemmon, D.: Increased amplitude of atmospheric rivers and associated extreme precipitation in ultra-high-resolution greenhouse warming simulations, *Communications Earth & Environment* 2023 4:1, 4, 313-, <https://doi.org/10.1038/s43247-023-00963-7>, 2023.
- Niittynen, P., Heikkinen, R. K., and Luoto, M.: Decreasing snow cover alters functional composition and diversity of Arctic tundra, *Proc. Natl. Acad. Sci. U. S. A.*, 117, 21480–21487, <https://doi.org/10.1073/pnas.2001254117>, 2020.
- EBAS database, NILU:
- Noël, B., Jakobs, C. L., van Pelt, W. J. J., Lhermitte, S., Wouters, B., Kohler, J., Hagen, J. O., Luks, B., Reijmer, C. H., van
560 de Berg, W. J., and van den Broeke, M. R.: Low elevation of Svalbard glaciers drives high mass loss variability, *Nat. Commun.*, 11, 4597-, <https://doi.org/10.1038/s41467-020-18356-1>, 2020.
- Norwegian Centre for Climate Services: Observations and weather statistics - Seklima, <https://seklima.met.no/observations/>.
- Norwegian Polar Institute: Kartdata Svalbard 1:100 000 (S100 Kartdata) / Map Data [Dataset]. Norwegian Polar Institute., 2014.
- 565 Nygård, T., Vihma, T., Birnbaum, G., Hartmann, J., King, J., Lachlan-Cope, T., Ladkin, R., Lüpkes, C., and Weiss, A.: Validation of eight atmospheric reanalyses in the Antarctic Peninsula region, *Quarterly Journal of the Royal Meteorological Society*, 142, 684–692, <https://doi.org/10.1002/qj.2691>, 2016.
- Payne, A. E., Demory, M. E., Leung, L. R., Ramos, A. M., Shields, C. A., Rutz, J. J., Siler, N., Villarini, G., Hall, A., and Ralph, F. M.: Responses and impacts of atmospheric rivers to climate change, *Nature Reviews Earth & Environment* 2020
570 1:3, 1, 143–157, <https://doi.org/10.1038/s43017-020-0030-5>, 2020.
- Peeters, B., Pedersen, Å. Ø., Loe, L. E., Isaksen, K., Veiberg, V., Stien, A., Kohler, J., Gallet, J. C., Aanes, R., and Hansen, B. B.: Spatiotemporal patterns of rain-on-snow and basal ice in high Arctic Svalbard: detection of a climate-cryosphere regime shift, *Environmental Research Letters*, 14, 015002, <https://doi.org/10.1088/1748-9326/aaefb3>, 2019.
- Van Pelt, W. J. J., Pohjola, V. A., and Reijmer, C. H.: The changing impact of snow conditions and refreezing on the mass balance of an idealized svalbard glacier, *Front. Earth Sci. (Lausanne)*, 4, 227264, <https://doi.org/10.3389/feart.2016.00102>,
2016.
- Van Pelt, W. and Frank, T.: New glacier thickness and bed topography maps for Svalbard, *Cryosphere*, 19, 1–17, <https://doi.org/10.5194/tc-19-1-2025>, 2025.



- Van Pelt, W. and Kohler, J.: Modelling the long-term mass balance and firn evolution of glaciers around Kongsfjorden, Svalbard, *Journal of Glaciology*, 61, 731–744, <https://doi.org/10.3189/2015JoG14J223>, 2015.
- Rantanen, M., Karpechko, A. Y., Lipponen, A., Nordling, K., Hyvärinen, O., Ruosteenoja, K., Vihma, T., and Laaksonen, A.: The Arctic has warmed nearly four times faster than the globe since 1979, *Commun. Earth Environ.*, 3, 168, <https://doi.org/10.1038/s43247-022-00498-3>, 2022.
- RGI 7.0 Consortium: Randolph Glacier Inventory - A Dataset of Global Glacier Outlines, Version 7.0. Boulder, Colorado USA. NSIDC: National Snow and Ice Data Center, 2023.
- Rinke, A., Segger, B., Crewell, S., Maturilli, M., Naakka, T., Nygård, T., Vihma, T., Alshawaf, F., Dick, G., Wickert, J., Keller, J., Rinke, A., Segger, B., Crewell, S., Maturilli, M., Naakka, T., Nygård, T., Vihma, T., Alshawaf, F., Dick, G., Wickert, J., and Keller, J.: Trends of Vertically Integrated Water Vapor over the Arctic during 1979–2016: Consistent Moistening All Over?, *J. Clim.*, 32, 6097–6116, <https://doi.org/10.1175/JCLI-D-19-0092.1>, 2019.
- Salzano, R., Cerrato, R., Scoto, F., Spolaor, A., Valentini, E., Salvatore, M., Esposito, G., Sapio, S., Taramelli, A., and Salvatori, R.: Detection of Winter Heat Wave Impact on Surface Runoff in a Periglacial Environment (Ny-Ålesund, Svalbard), *Remote Sens. (Basel)*, 15, <https://doi.org/10.3390/rs15184435>, 2023.
- Sasgen, I., Steinhöfel, G., Kasprzyk, C., Matthes, H., Westermann, S., Boike, J., and Grosse, G.: Atmosphere circulation patterns synchronize pan-Arctic glacier melt and permafrost thaw, *Communications Earth & Environment* 2024 5:1, 5, 375–, <https://doi.org/10.1038/s43247-024-01548-8>, 2024.
- Scholz, S. R. and Lora, J. M.: Atmospheric rivers cause warm winters and extreme heat events, *Nature* 2024 636:8043, 636, 640–646, <https://doi.org/10.1038/s41586-024-08238-7>, 2024.
- Schuler, T. V., Kohler, J., Elagina, N., Hagen, J. O. M., Hodson, A. J., Jania, J. A., Kääb, A. M., Luks, B., Małeck, J., Moholdt, G., Pohjola, V. A., Sobota, I., and Van Pelt, W. J. J.: Reconciling Svalbard Glacier Mass Balance, *Front. Earth Sci. (Lausanne)*, 8, 523648, <https://doi.org/10.3389/feart.2020.00156>, 2020.
- Sobota, I., Weckwerth, P., and Grajewski, T.: Rain-On-Snow (ROS) events and their relations to snowpack and ice layer changes on small glaciers in Svalbard, the high Arctic, *J. Hydrol. (Amst)*, 590, 125279, <https://doi.org/10.1016/J.JHYDROL.2020.125279>, 2020.
- Thaker, R., Vavrus, S. J., Shields, C. A., DuVivier, A. K., MacLennan, M., Holland, M. M., and Landrum, L.: Arctic Atmospheric Rivers in a Changing Climate and the Impacts on Sea Ice, *Journal of Geophysical Research: Atmospheres*, 130, e2024JD042521, <https://doi.org/10.1029/2024JD042521>, 2025.
- Vickers, H., Mooney, P., and Landgren, O.: Recent and projected changes in rain-on-snow event characteristics across Svalbard, *Cryosphere*, 19, 6907–6926, <https://doi.org/10.5194/tc-19-6907-2025>, 2025.
- Walbröl, A., Michaelis, J., Becker, S., Dorff, H., Ebell, K., Gorodetskaya, I., Heinold, B., Kirbus, B., Lauer, M., Mahernld, N., Maturilli, M., Mayer, J., Müller, H., Neggers, R. A. J., Paulus, F. M., Röttenbacher, J., Rückert, J. E., Schirmacher, I., Slättberg, N., Ehrlich, A., Wendisch, M., and Crewell, S.: Contrasting extremely warm and long-lasting cold air anomalies in



- the North Atlantic sector of the Arctic during the HALO-(AC)3 campaign, *Atmos. Chem. Phys.*, 24, 8007–8029, <https://doi.org/10.5194/ACP-24-8007-2024>, 2024.
- 615 Wang, Z., Ding, Q., Wu, R., Ballinger, T. J., Guan, B., Bozkurt, D., Nash, D., Baxter, I., Topál, D., Li, Z., Huang, G., Chen, W., Chen, S., Cao, X., and Chen, Z.: Role of atmospheric rivers in shaping long term Arctic moisture variability, *Nature Communications* 2024 15:1, 15, 5505–, <https://doi.org/10.1038/s41467-024-49857-y>, 2024.
- Wedum, A. E., Pettersen, C., Guy, H., Gallagher, M. R., Shupe, M. D., and Mattingly, K. S.: Impacts of Atmospheric Rivers in Central Greenland: Snowfall, Clouds, and Atmospheric State, *Journal of Geophysical Research: Atmospheres*, 131, e2025JD044309, <https://doi.org/10.1029/2025JD044309>, 2026.
- 620 WGMS: Fluctuations of Glaciers (FoG) Database. World Glacier Monitoring Service (WGMS), <https://doi.org/10.5904/WGMS-FOG-2016-08>, 2025.
- Yamagata, S., Kobayashi, D., Ohta, S., Murao, N., Shiobara, M., Wada, M., Yabuki, M., Konishi, H., and Yamanouchi, T.: Properties of aerosols and their wet deposition in the arctic spring during ASTAR2004 at Ny-Alesund, Svalbard, *Atmos. Chem. Phys.*, 9, 261–270, <https://doi.org/10.5194/acp-9-261-2009>, 2009.
- 625 Zhang, P., Chen, G., Ting, M., Ruby Leung, L., Guan, B., and Li, L.: More frequent atmospheric rivers slow the seasonal recovery of Arctic sea ice, *Nat. Clim. Chang.*, 13, 266–273, <https://doi.org/10.1038/s41558-023-01599-3>, 2023.